

Abnormal thermal conduction in argyrodite-type $\text{Ag}_9\text{FeS}_{6-x}\text{Te}_x$ materials

HPSTAR
1249-2021



Z. Jin^{a,b}, Y. Xiong^{a,d}, K. Zhao^{c,*}, H. Dong^d, Q. Ren^e, H. Huang^{a,b}, X. Qiu^{a,b}, J. Xiao^a, P. Qiu^a, L. Chen^{a,b}, X. Shi^{a,b,**}

^a State Key Laboratory of High Performance Ceramics and Superfine Microstructure, Shanghai Institute of Ceramics, Chinese Academy of Sciences, Shanghai, 200050, China

^b Center of Materials Science and Optoelectronics Engineering, University of Chinese Academy of Sciences, Beijing, 100049, China

^c State Key Laboratory of Metal Matrix Composites, School of Materials Science and Engineering, Shanghai Jiao Tong University, Shanghai, 200240, China

^d Center for High Pressure Science and Technology Advanced Research, Shanghai, 201203, China

^e China Spallation Neutron Source, Institute of High Energy Physics, Chinese Academy of Sciences, Beijing, 100049, China

ARTICLE INFO

Article history:

Received 17 January 2021

Received in revised form

16 March 2021

Accepted 7 April 2021

Available online 20 April 2021

Keywords:

Thermal conductivity

Chemical bonds

Glass-like

Argyrodite

Einstein oscillators

ABSTRACT

Rationalizing the underlying mechanism that correlates phonon transport with structural complexity is crucial for the development of materials with ultralow thermal conductivity. Herein, we investigated the abnormal thermal transport and lattice dynamics in $\text{Ag}_9\text{FeS}_{6-x}\text{Te}_x$ argyrodite-type compounds via a combination of properties characterization, model analysis, and theoretical calculations. Our results show that the ordered α -phase and disordered β -phase of $\text{Ag}_9\text{FeS}_{6-x}\text{Te}_x$ exhibit distinct temperature dependency of lattice thermal conductivity κ_L . Specifically, the κ_L of ordered α -phase shows a crystalline characteristic with a pronounced Umklapp peak observed at ~ 10 K, while the κ_L of disordered β -phase monotonously increases in the whole temperature range without a peak or plateau. Such different thermal transport behavior is a result of different contributions to the reduction of κ_L from the structural disorder and the low-lying multi-Einstein oscillators, both of which are associated with the weakly bonded Ag^+ ions. The knowledge depicted here provides fundamental insights into the extraordinary thermal transports in materials with structural disorder and/or weak chemical bonds.

© 2021 Elsevier Ltd. All rights reserved.

1. Introduction

Thermal conductivity, one of the most fundamental properties, refers to the ability of a material to transfer or conduct heat through both phonons and electrons. Materials with low thermal conductivity have gained great attention in a great diversity of research fields, such as thermal insulators, thermal barrier coatings, thermoelectric materials, and so on [1–5]. The total thermal conductivity (κ) is generally composed of electronic thermal conductivity (κ_e) and lattice thermal conductivity (κ_L). The former part, κ_e , is proportional to the material's electrical conductivity and thus is high in metals but negligible in electrically insulating solids. The

latter part, κ_L , can be described as $\kappa_L = 1/3C_v v l$, where C_v , v , and l stand for the specific heat at constant volume, the group velocity of phonon, and the phonon mean free path, respectively. Theoretically, l can be shortened by various scattering events but C_v and v are the intrinsic properties and difficult to alter. Thus, the common strategy for reducing κ_L of a material is to reduce l by intensifying phonon scattering, while only a few studies focus on the manipulation of C_v or v . Over the past decades, a variety of approaches, such as all-scale hierarchical structuring [6,7], entropy engineering [8,9], liquid-like ions [10–13], and lattice strain engineering [14,15], have been extensively developed to reduce the lattice thermal conductivity. Moreover, a lot of materials with intrinsically low κ_L have also been explored, in which κ_L is closely related to the structural complexity, chemical bonding nature, and bonding environments [16–19]. For instance, compounds with lone pair electrons or hierarchical chemical bonds usually have large lattice anharmonicity, resulting in strong phonon-phonon interactions and hence lower κ_L [20,21]. Besides, materials with soft chemical bonds generally have a low sound velocity and a high Gruneisen parameter, which, in

* Corresponding author.

** Corresponding author. State Key Laboratory of High Performance Ceramics and Superfine Microstructure, Shanghai Institute of Ceramics, Chinese Academy of Sciences, Shanghai, 200050, China.

E-mail addresses: zkp.1989@sjtu.edu.cn (K. Zhao), xshi@mail.sic.ac.cn (X. Shi).

turn, give rise to an intrinsic ultralow κ_L [18,22–25]. Therefore, exploring novel compounds with intrinsically low κ_L and rationalizing the nature of their chemical bonding are crucial for the design of efficient energy materials.

Recently, the mineral argyrodite-type compounds have drawn great attention as a new family of promising thermoelectric materials. The argyrodites contain a large family of compounds with a general chemical formula $A_{12-y/x}^{+}B^{y+}Q_6^{2-}$ ($A = \text{Li, Cu, Ag}$; $B = \text{Ga, Al, Fe, Si, Ge, Sn, P, As}$; $Q = \text{S, Se, Te}$) [11,18,23–31]. These compounds typically show rich phase transition behavior. At high temperature, they usually crystallize in high-symmetry disordered structures, wherein A^+ ions are highly mobile and exhibit liquid-like characteristic. At low temperature, they transform into ordered monoclinic, orthogonal, or hexagonal structures, depending on their chemical compositions. The A^+ ions at these low temperature phases display highly ordered distributions, which is in contrast to the disordered A^+ at high temperature phases. Very low sound velocity and cutoff frequency of acoustic phonons are found in these argyrodite materials, stemming from their weakly bonded A^+ and large unit cells [18,23,25,31]. More importantly, extremely low κ_L values have been reported in most argyrodite-type compounds, such as $0.23 \text{ W m}^{-1} \text{ K}^{-1}$ in Ag_9GaSe_6 [30], $0.25 \text{ W m}^{-1} \text{ K}^{-1}$ in Cu_7PSe_6 [29], and $0.15 \text{ W m}^{-1} \text{ K}^{-1}$ in Ag_8SnSe_6 [25]. The ‘liquid-like’ behavior of disordered A^+ ions at high temperatures is believed the main origin of the low κ_L in disordered phases [13]. However, the κ_L is also very low at low temperatures, at which all the ions are frozen out, leading to very weak liquid-like behavior. The thermal transport behavior is different from both crystalline and amorphous compounds, which is quite abnormal and special. Moreover, the κ_L for the ordered argyrodites is also quite low, but the mechanism is rarely investigated.

Herein, we focus on an iron-containing argyrodite-type compound, $\text{Ag}_9\text{FeS}_{6-x}\text{Te}_x$, which has an ordered α -phase and a disordered β -phase that possess the same elements but very different thermal transports. Both phases show intrinsically ultralow κ_L values in the whole temperature range. In particular, the κ_L in disordered β -phase monotonously increases from $0.03 \text{ W m}^{-1} \text{ K}^{-1}$ at 3 K to $0.3 \text{ W m}^{-1} \text{ K}^{-1}$ at 300 K and maintains such low values up to 800 K. In contrast, the κ_L in ordered α -phase shows a distinct peak at around 10 K. Through both experimental measurements and theoretical calculations, we reveal such difference is correlated with the different contributions to the reduction of κ_L from the structural disorder and the low energy multi-Einstein optic modes, originating from the weakly bonded Ag. This work can shed light on the origin of ultralow κ_L in other argyrodite-type compounds.

2. Experimental section

2.1. Synthesis

Polycrystalline samples of $\text{Ag}_9\text{FeS}_{6-x}\text{Te}_x$ ($x = 0.3, 0.5, 1.0, 1.5, 2.0, 2.3$) were prepared by a melting-quenching-annealing-sintering process. High-purity elements of Ag (shots, 99.9999%, Alfa Aesar), Fe (granules, 99.98%, Alfa Aesar), S (pieces, 99.9995%, Alfa Aesar), and Te (powders, 99.999%, Alfa Aesar) were weighed in stoichiometric proportions and then sealed in silica tubes under vacuum. The tubes were heated to 1273 K in 12 h and held at this temperature for 12 h followed by a quenching process. In order to ensure uniform distribution of the elements, the quenched tubes were annealed at 773 K for 6 days. Finally, the obtained ingots were handed ground into fine powders and then consolidated into dense pellets by hot pressing at 873 K under a pressure of 65 MPa. The density of resulting samples is higher than 97% of theoretical value.

2.2. Characterization

The phase purity and crystal structure of the synthesized $\text{Ag}_9\text{FeS}_{6-x}\text{Te}_x$ polycrystalline samples were examined by powder X-ray diffraction (PXRD, Rint 2000, Rigaku, Japan) using $\text{Cu K}\alpha$ radiation ($\lambda = 1.5405 \text{ \AA}$) at room temperature. The phase transition characters were analyzed by differential scanning calorimetric (DSC, Netzsch 200 F3) and low temperature powder X-ray diffraction ($\lambda = 1.5405 \text{ \AA}$) measurements. The Rietveld refinements were performed using FULLPROF program. The sample microstructure and chemical composition were measured by scanning electron microscopy (SEM, ZEISS Supra 55) equipped with energy dispersive spectrometer (EDS, Oxford Horiba 250). The electron backscattered diffraction (EBSD) analysis was performed on field emission scanning electron microscope (FESEM, Verios G4). The details of microstructure were further examined by transmission electron microscope (TEM, JEM-2100F). Optical diffuse reflectance spectra of powder samples were obtained at room temperature using U-4100 Spectrophotometer, with the collecting range from 250 to 2600 nm at a scan rate of 600 nm/min. The thermal diffusivity (D) above 300 K was measured by laser flash method using Netzsch LFA 457 under continuous argon flow, and the samples were spray-coated with a thin layer of graphite before the measurement to minimize the reflectivity. The thermal conductivity (κ) was calculated via $\kappa = D C_p \rho$, where the density (ρ) was determined using the Archimedes method, and the heat capacity (C_p) was estimated by the Dulong Petit limit. Low-temperature (2.5–300 K) heat capacity and thermal transport measurements were performed on Quantum Design physical property measurement system (PPMS). The transverse and longitudinal sound velocities of the samples were obtained by the ultrasonic pulse method on Advanced Ultrasonic Measurement System at room temperature.

2.3. Theoretical calculations

Lattice dynamics were investigated using Density Functional theory (DFT) based on the modified low-temperature crystal structure of $\text{Ag}_9\text{FeS}_4\text{Te}_2$. Crystal structure and electronic structure optimization were performed using the projector-augmented wave (PAW) method, which is implemented in the Vienna ab initio simulation package (VASP), choosing the Perdew-Burke-Ernzerhof (PBE)-type generalized gradient approximation (GGA) as the exchange-correlation functional [32]. The plane-wave energy cutoff was set at 450 eV. In order to get the most stable structure in calculations, all the atomic positions were relaxed until the calculated Hellmann-Feynman force on each atom of the unit cell was less than 10^{-6} eV/\AA . Using the finite displacement method, the relaxed crystal was used for static calculation with the package phonyopy [33]. We constructed a $2 \times 2 \times 2$ supercell (including 224 atoms) and set convergence criteria of electronic step as 10^{-8} eV/\AA for static calculation of displaced supercell in accurate precision. After all displaced supercells had converged, sound velocity can be acquired by averaging gamma points’ phonon group velocities along different directions. This case has not considered the spin-orbit coupling (SOC) effect.

3. Results and discussion

The crystal structure and phase transition of $\text{Ag}_9\text{FeS}_{4.1}\text{Te}_{1.9}$ have been investigated by Frank et al. [27]. As depicted in Fig. 1a, it crystallizes in a cubic structure (β -phase) with space group of $F\bar{4}3m$ above 265 K. The Ag^+ ions in this structure are disorderly distributed and highly mobile, suggesting their weakly bonding with S/Te anions. With temperature decreasing to below 265 K, the high-

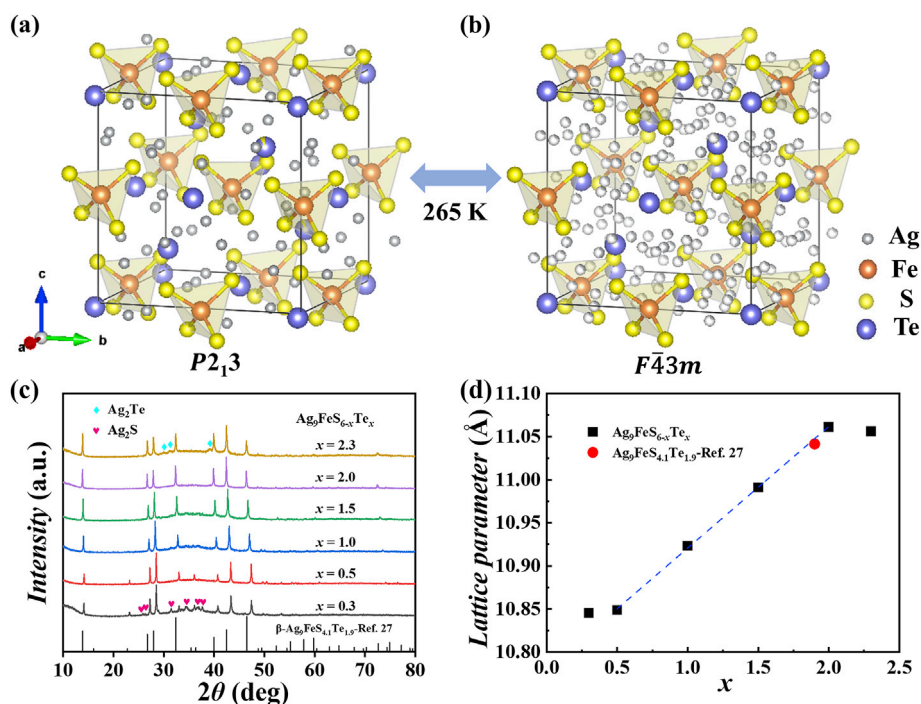


Fig. 1. Visualization of the (a) low-temperature ($P2_13$) and (b) high-temperature ($F\bar{4}3m$) crystal structures for $Ag_9FeS_{4.1}Te_{1.9}$. The partial site occupancy is indicated by partial coloring of the atoms. (c) Room-temperature powder X-ray diffraction patterns for $Ag_9FeS_{6-x}Te_x$ ($x = 0.3, 0.5, 1.0, 1.5, 2.0, 2.3$) samples. The theoretical diffraction peaks of high-temperature phase for $Ag_9FeS_{4.1}Te_{1.9}$ are taken from Ref. 27. (d) Lattice parameters calculated by structural Rietveld refinements for $Ag_9FeS_{6-x}Te_x$ samples at room temperature. The lattice parameter of $Ag_9FeS_{4.1}Te_{1.9}$ taken from Ref. 27 is included for comparison.

temperature β -phase is converted to a low-temperature α -phase with space group of $P2_13$. It should be noted that the anion framework of α -phase is scarcely changed as compared with β -phase. Besides, the lattice parameters and Ag–S/Te bond length for both low- and high-temperature phases are very close. Therefore, it is believed that Ag^+ ions are also loosely bonded in the low-temperature α -phase although the Ag^+ ions are located in an ordered fashion. Herein we synthesized a series of $Ag_9FeS_{6-x}Te_x$ samples with x ranging from 0.3 to 2.3. The measured powder XRD patterns are shown in Fig. 1c and Fig. S1. When x is between 0.5 and 2.0, all diffraction peaks of $Ag_9FeS_{6-x}Te_x$ samples are well indexed to the cubic β -phase described above. However, some additional peaks belonging to either Ag_2S or Ag_2Te phases are observed when x is 0.3 or 2.3. This suggests that $Ag_9FeS_{6-x}Te_x$ is stable in a wide composition range with x between 0.5 and 2.0. Beyond this range, the structure is unstable and impurity phases will form. The lattice parameters determined by Rietveld refinements are plotted in Fig. 1d. As expected, with increasing Te content, the lattice parameters gradually increase since the ionic radius of Te^{2-} (2.21 Å) is much larger than that of S^{2-} (1.84 Å). The lattice parameters almost linearly increase with increasing x from 0.5 to 2.0, well obeying the Vegard's law. This implies that part Te atoms successfully enter the S lattice sites or part S atoms enter the Te lattice sites. However, at a lower ($x = 0.3$) or higher ($x = 2.3$) Te content, the lattice parameters obviously deviate off the Vegard's law. Our scanning electron microscopy, energy dispersive spectroscopy, and transmission electron microscopy measurements also demonstrate the samples with $x = 0.5, 1.0$ and 1.5 are single phased without detectable impurity phases (see Fig. S2). All the evidences corroborate that the Te solubility limit in $Ag_9FeS_{6-x}Te_x$ is between $x = 0.5$ and 2.0.

To investigate the influence of Te alloying on phase transition characters, the differential scanning calorimetric (DSC), low-temperature powder XRD measurements, and Rietveld refinement analysis were performed on $Ag_9FeS_{6-x}Te_x$ samples. As

depicted in Fig. 2a, an obvious endothermic peak is observed in the DSC curve of $Ag_9FeS_4Te_2$, corresponding to the phase transition from ordered α -phase to disordered β -phase. The phase transition temperature for $Ag_9FeS_4Te_2$ is around 270 K, which is very close to the value (265 K) reported by Frank et al. [27]. This is further demonstrated by our low-temperature XRD and Rietveld refinement results shown in Fig. 2b, Fig. S3 and Table S1. At 100 K and 200 K, nearly all the diffraction peaks can be well indexed to the ordered α -phase, pointing to the structural transformation during cooling. However, when the Te content is decreased to below $x = 1.5$, no phase transition peak but a weak hump is observed, as illustrated in Fig. 2a and Fig. S4. This suggests the initial phase transition character of $Ag_9FeS_4Te_2$ is altered when decreasing the Te content. Nearly all the diffraction peaks can be still identified to the β -phase when decreasing the temperature from 300 K to 100 K (see Fig. 2c and Fig. S3). Therefore, we believe the crystal structure of samples with $x \leq 1.5$ is only slightly modified and the weak hump is caused by the local rearrangement of Ag^+ ions. The retention of disordered β -phase down to low temperature may be related to the large atomic size difference between S and Te, which chemically quenches the Ag^+ ions into an amorphous state [34].

Fig. 3a shows the lattice thermal conductivity κ_L above 300 K for $Ag_9FeS_{6-x}Te_x$, in comparison with some typical thermoelectric materials. The total thermal conductivity κ is almost the same as κ_L because the electrical conductivity of $Ag_9FeS_{6-x}Te_x$ is quite low ($< 10^2 \text{ S m}^{-1}$), resulting in negligible electronic thermal conductivity κ_e . All $Ag_9FeS_{6-x}Te_x$ samples exhibit intrinsically ultralow κ_L with values between 0.2–0.3 $\text{W m}^{-1} \text{ K}^{-1}$, which is even lower than the theoretical minimum lattice thermal conductivity ($\kappa_L \sim 0.37 \text{ W m}^{-1} \text{ K}^{-1}$) estimated by Cahill's model. Such low values are comparable to those observed in other argyrodite-type compounds like Cu_8GeSe_6 [28] and Ag_9GaSe_6 [30], but much lower than those of state-of-the-art thermoelectric materials such as Bi_2Te_3 [35], $PbTe$ [36], Mg_3Sb_2 [37] and Cu_2Se [12]. Particularly, κ_L of

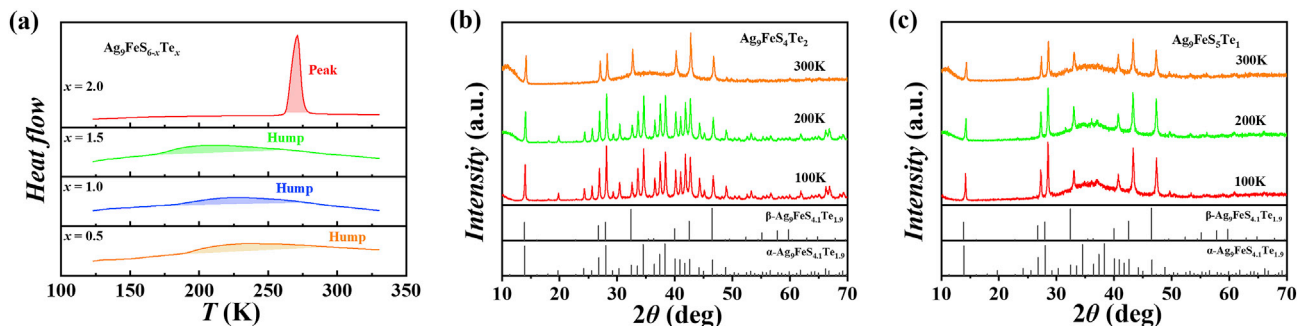


Fig. 2. (a) Measured DSC curves for $\text{Ag}_9\text{FeS}_{6-x}\text{Te}_x$ ($x = 0.5, 1.0, 1.5, 2.0$) samples from 125 K to 330 K. Temperature dependent powder XRD patterns for (b) $\text{Ag}_9\text{FeS}_4\text{Te}_2$ and (c) $\text{Ag}_9\text{FeS}_5\text{Te}_1$ at 100 K, 200 K, and 300 K.

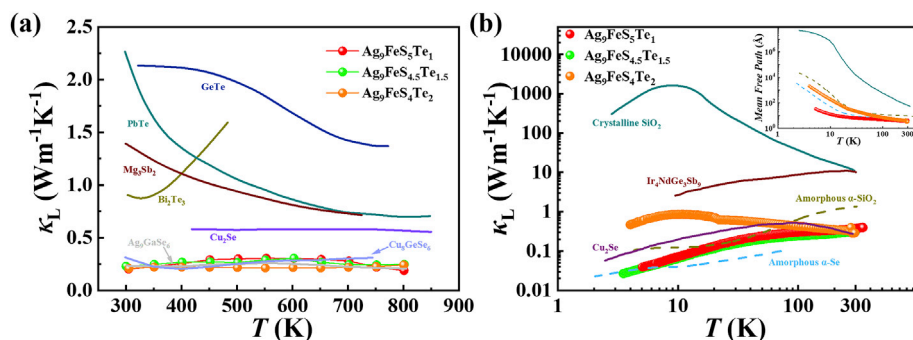


Fig. 3. (a) The lattice thermal conductivity (κ_L) for $\text{Ag}_9\text{FeS}_{6-x}\text{Te}_x$ ($x = 1.0, 1.5, 2.0$) from 300 K to 800 K. The data of some typical thermoelectric materials (GeTe [54], PbTe [36], Mg_3Sb_2 [37], Bi_2Te_3 [35], Cu_2Se [12], Cu_8GeSe_6 [28], Ag_9GaSe_6 [30]) are included for comparison. (b) Low temperature (3.5–300 K) lattice thermal conductivity (κ_L) for $\text{Ag}_9\text{FeS}_{6-x}\text{Te}_x$ ($x = 1.0, 1.5, 2.0$). Noteworthy, $\text{Ag}_9\text{FeS}_5\text{Te}_1$ and $\text{Ag}_9\text{FeS}_{4.5}\text{Te}_{1.5}$ crystallize in disordered β -phase while $\text{Ag}_9\text{FeS}_4\text{Te}_2$ crystallizes in ordered α -phase below 200 K. The data of crystalline SiO_2 [55], $\text{Ir}_4\text{NdGe}_3\text{Sb}_9$ [41], Cu_2Se [56], amorphous α -Se [42] and α - SiO_2 [57] are also plotted for comparison. The inset shows the estimated mean free path as a function of temperature [42].

$\text{Ag}_9\text{FeS}_{6-x}\text{Te}_x$ is nearly temperature independent, which is in stark contrast to the T^{-1} dependence of normal crystalline compounds with Umklapp scattering as the major scattering mechanism. Considering its proper band gap (see Fig. S5), $\text{Ag}_9\text{FeS}_{6-x}\text{Te}_x$ may be a promising thermoelectric material if the electrical transport properties can be further optimized.

Fig. 3b shows the temperature dependent κ_L for $\text{Ag}_9\text{FeS}_{6-x}\text{Te}_x$ at low temperatures. The data of some crystalline and amorphous materials are also plotted for comparison. Generally, a pronounced Umklapp peak (i.e. dielectric maximum) is observed in the κ_L of crystalline compounds, while a plateau emerges in the κ_L of amorphous materials at around 10 K [38]. Intriguingly, $x \leq 1.5$ and $x = 2$ samples exhibit very different phonon transport behavior (Fig. 3b), which might be attributed to their different crystal structures below 200 K. Similar to most crystalline materials, the κ_L of ordered $\text{Ag}_9\text{FeS}_4\text{Te}_2$ shows a perceptible peak at around 10 K. Nevertheless, the maximum value is merely $1.0 \text{ W m}^{-1} \text{ K}^{-1}$, which is still among the lowest κ_L values in bulk TE materials. Note that the κ_L of $\text{Ag}_9\text{FeS}_4\text{Te}_2$ is slightly reduced at around 22 K, which may be ascribed to the critical scattering of phonons during magnetic transitions [27,39]. Differing from both crystalline and amorphous materials, the κ_L of disordered $\text{Ag}_9\text{FeS}_{6-x}\text{Te}_x$ ($x = 1.0$ and 1.5) monotonously increases during the entire temperature range without a peak or plateau. Such abnormal κ_L behavior has been also observed in $\text{Cu}_2\text{S}_{1/3}\text{Se}_{1/3}\text{Te}_{1/3}$ and $\text{Ir}_4\text{NdGe}_3\text{Sb}_9$ [40,41]. The phonon mean free path (l) is derived using $\kappa_L = 1/3C_v v l$ and the results are shown in the inset of Fig. 3b. In the temperature range above 100 K, the phonon mean free paths for both $\text{Ag}_9\text{FeS}_5\text{Te}_1$ and $\text{Ag}_9\text{FeS}_4\text{Te}_2$ are scarcely changed with a constant value of $\sim 4.4 \text{ \AA}$, which approaches the average interatomic separation (2.7 \AA). Below 100 K,

the l of $\text{Ag}_9\text{FeS}_4\text{Te}_2$ gradually increases, similar to the trend of amorphous α - SiO_2 and α -Se [42]. The l of $\text{Ag}_9\text{FeS}_5\text{Te}_1$ also gradually increases with decreasing temperature, but its temperature dependency is in stark contrast to the much stronger temperature dependency observed in $\text{Ag}_9\text{FeS}_4\text{Te}_2$ and other crystalline or amorphous materials.

The distinct thermal transport characteristics in the ordered α -phase and disordered β -phase of $\text{Ag}_9\text{FeS}_{6-x}\text{Te}_x$ are believed to be caused by their different crystal structures, chemical bonding, and lattice dynamics. In the β -phase, Ag^+ ions are randomly distributed in the lattice sites, i.e., only part of the sites is occupied, resulting in the structural disorder of Ag sublattice. This has been well corroborated in the structural analysis. Combining the weak chemical bonding between Ag and S/Te, extremely low thermal conductivity is detected in the β -phase. In the α -phase, although all the ions including Ag^+ are ordered, the weak chemical bonding still exists due to the similar coordination environment and bond lengths between the α -phase and β -phase. The presence of weak chemical bonds can be ascertained by the ultralow speed of sound (v), low Debye temperature (Θ_D), and high Gruneisen parameter (γ) in $\text{Ag}_9\text{FeS}_{6-x}\text{Te}_x$. As listed in Table 1, the transverse and longitudinal

Table 1

Room temperature transverse (v_t), longitudinal (v_l) and average (v_{avg}) sound velocities, bulk module (B), shear module (G), Gruneisen parameter (γ) and Debye temperature (Θ_D) for $\text{Ag}_9\text{FeS}_5\text{Te}_1$, $\text{Ag}_9\text{FeS}_{4.5}\text{Te}_{1.5}$ and $\text{Ag}_9\text{FeS}_4\text{Te}_2$.

Samples	v_t (m/s)	v_l (m/s)	v_{avg} (m/s)	B (GPa)	G (GPa)	γ	Θ_D (K)
$\text{Ag}_9\text{FeS}_5\text{Te}_1$	1100	2855	1247	43.9	8.1	2.8	136.1
$\text{Ag}_9\text{FeS}_{4.5}\text{Te}_{1.5}$	1094	2851	1241	44.5	8.2	2.8	134.4
$\text{Ag}_9\text{FeS}_4\text{Te}_2$	1082	2847	1227	45.5	8.1	2.8	132.2

speeds of sound for $\text{Ag}_9\text{FeS}_{4.5}\text{Te}_{1.5}$ are 1094 and 2851 m/s, respectively, giving rise to an average v of 1241 m/s, which is among the lowest values of all known solid materials. The Debye temperature, calculated on the basis of the above sound velocities, is only 136.1 K for $\text{Ag}_9\text{FeS}_5\text{Te}_1$, 134.4 K for $\text{Ag}_9\text{FeS}_{4.5}\text{Te}_{1.5}$ and 132.2 K for $\text{Ag}_9\text{FeS}_4\text{Te}_2$. These values are also lower than most of the state-of-the-art thermoelectric materials. The Gruneisen parameter, reflecting the lattice vibrational anharmonicity, is calculated as high as 2.8 for $\text{Ag}_9\text{FeS}_5\text{Te}_1$, $\text{Ag}_9\text{FeS}_{4.5}\text{Te}_{1.5}$ and $\text{Ag}_9\text{FeS}_4\text{Te}_2$. All of these results are the important signatures of the weakly bonding of Ag to its surrounding S/Te atoms [43,44].

Generally, weak chemical bonds signify large oscillation amplitudes and thus result in the presence of low-lying phonon modes. To prove our conjecture, we measured the low-temperature heat capacity for $\text{Ag}_9\text{FeS}_{4.5}\text{Te}_{1.5}$ and $\text{Ag}_9\text{FeS}_4\text{Te}_2$ (Fig. 4a). It is clear that the C_p/T^3 vs T curves for both compounds exhibit a strong Boson peak, which is the signature of excess low-frequency vibrational modes that usually observed in amorphous or disordered materials [45]. Moreover, the maximum value of Boson peak is much higher in $\text{Ag}_9\text{FeS}_{4.5}\text{Te}_{1.5}$ than that in $\text{Ag}_9\text{FeS}_4\text{Te}_2$, implying more low-lying optical modes excited in the temperature range of 2–14 K. We fitted the experimental C_p data with the modified Debye-Einstein model [46]:

$$C_p/T = \phi + \beta T^2 + \sum_i \left(A_i (\Theta_{E_i})^2 \beta (T^2)^{-\frac{3}{2}} \cdot \frac{e^{\frac{\Theta_{E_i}}{T}}}{(e^{\frac{\Theta_{E_i}}{T}} - 1)^2} \right)$$

Here, the first term ϕ , second term βT^2 , and the last summation term denote the electronic contribution, Debye lattice contribution, and Einstein oscillator contribution, respectively. A_i and Θ_{E_i} are the prefactor and characteristic temperature for the i th Einstein oscillator mode, respectively. The fitting curves are presented in Fig. 4 and Fig. S6, and related parameters are listed in Tables S2 and S3. Clearly, the traditional Debye model alone can't describe the experimental data, while one Debye mode plus 3 Einstein modes is required to best fit the experimental heat capacity for both

$\text{Ag}_9\text{FeS}_{4.5}\text{Te}_{1.5}$ and $\text{Ag}_9\text{FeS}_4\text{Te}_2$ (Fig. S6). These results well corroborate the existence of low-energy optical modes originating from weakly bonded Ag in $\text{Ag}_9\text{FeS}_{6-x}\text{Te}_x$. In comparison to the ordered $\text{Ag}_9\text{FeS}_4\text{Te}_2$ compound, the disordered $\text{Ag}_9\text{FeS}_{4.5}\text{Te}_{1.5}$ possesses lower Einstein temperature and thus lower phonon energy of Einstein modes (see Tables S2 and S3).

To gain further insight and confidence in our experimental and modelling results, we have performed theoretical calculations on the phonon dispersion and phonon density of states (PDOS) of the ordered α -phase. The theoretical calculation on the β -phase is unfeasible at current stage due to its disordered nature. As shown in Fig. 4d, the lowest optical phonon mode located at the X-M direction is only 2.2 meV, which is in reasonable agreement with our fitting results from heat capacity. The dispersionless optical phonon modes above 2.2 meV contribute little to the phonon transport due to their very low sound velocities. Besides, the low-frequency optical modes overlap with the acoustic branches, rendering acoustic-optical interactions. By projecting the PDOS of $\text{Ag}_9\text{FeS}_4\text{Te}_2$ onto different atomic species (see Fig. 4d), it is found that most of the low-frequency phonon modes are contributed by the Ag atoms, further confirming our argue that Ag atoms are weakly bonded. The theoretical sound velocities calculated from phonon dispersions are 1421, 1430, 3293 m/s for the two transverse and one longitudinal acoustic phonons, respectively. These values are slightly higher than our experimental results of β -phase at room temperature. Overall, the weak chemical bonding between Ag and S/Te contributes to low sound velocity, large Gruneisen parameter, and especially the low-lying optical phonons, consequently resulting in the unusual thermal transports.

Weak chemical bonds usually lead to low-lying phonons and thus result in the phonon resonant scattering, while structural disorder not only alter the scattering events but also change the phonon group velocities. To better assess the contributions of phonon resonant scattering and structural disorder scattering to κ_L , we use the Debye-Callaway model to fit the low-temperature experimental κ_L of disordered $\text{Ag}_9\text{FeS}_{4.5}\text{Te}_{1.5}$ and ordered $\text{Ag}_9\text{FeS}_4\text{Te}_2$. This model can be written as [47,48]:

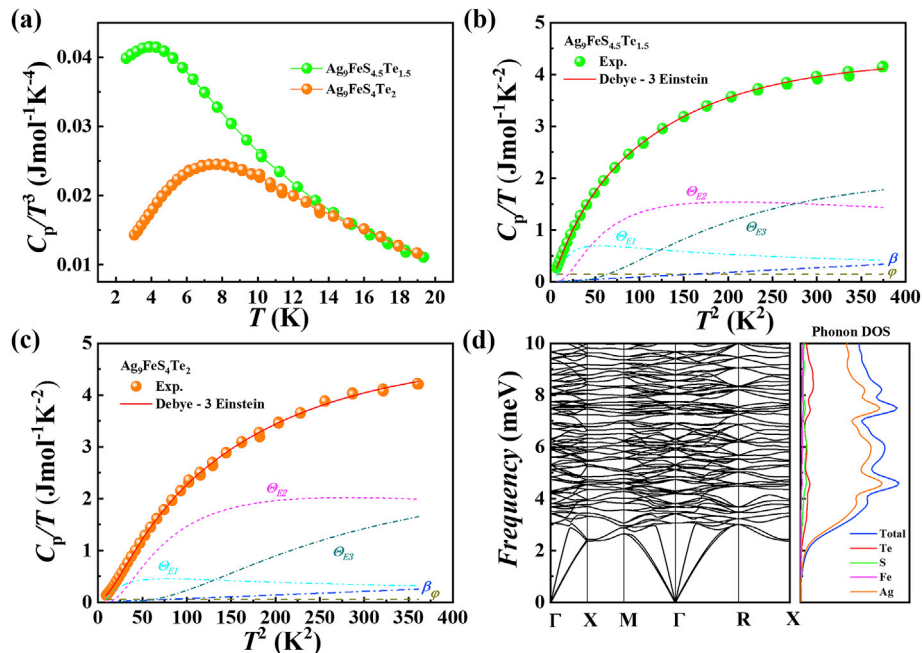


Fig. 4. (a) Measured heat capacity plotted as C_p/T^3 versus T for $\text{Ag}_9\text{FeS}_{4.5}\text{Te}_{1.5}$ and $\text{Ag}_9\text{FeS}_4\text{Te}_2$ from 2.5 K to 20 K. Fitted curves by using one Debye mode and 3 Einstein modes for (b) $\text{Ag}_9\text{FeS}_{4.5}\text{Te}_{1.5}$ and (c) $\text{Ag}_9\text{FeS}_4\text{Te}_2$. (d) Calculated phonon dispersion relations and phonon density of states for the ordered α -phase of $\text{Ag}_9\text{FeS}_4\text{Te}_2$.

$$\kappa_L = \frac{k_B}{2\pi^2 v_{avg}} \left(\frac{k_B T}{\hbar} \right)^3 \int_0^{\theta_D/T} \frac{x^4 e^x}{\tau_c^{-1} (e^x - 1)^2} dx$$

where $x = \hbar\omega/k_B T$, which is defined as reduced phonon frequency, ω is the phonon frequency, τ_c is the total relaxation time, k_B is the Boltzmann constant and \hbar is the reduced Planck constant. Considering the phonon scattering from grain boundary (B), point defect (PD), Umklapp process (U), structural disorder (D) [49] and phonon resonance (RE), the overall τ_c can be expressed as [48]:

$$\tau_c^{-1} = \frac{v_{avg}}{L} + A\omega^4 + B\omega^2 Te^{-\theta_D/3T} + E\omega^2 + \sum \frac{C_i \omega^2}{(\omega_i^2 - \omega^2)^2}$$

in which L stands for average grain size, ω_i ($i = 1, 2, 3$) is the phonon resonance frequency, and A, B, E, C_i ($i = 1, 2, 3$) are the fitting parameters of PD, U, D and RE, respectively. We adopted various methods to constraint or fix most of the parameters to make the fitting more reliable. For the B term, we determined the grain size L by performing electron backscattered diffraction (EBSD) analysis on our samples. As shown in Fig. S7, the grain size is between 0.8–20 μm . Therefore, we constraint the parameter L within the range of 0.8–20 μm . For the PD term, we calculated the parameter A through the formula $A = V_0 (\Gamma_M + \Gamma_S)/(4\pi v_s^3)$, where V_0 is the unit cell volume, v_s is the mean sound velocity, and Γ_M and Γ_S are scattering parameters related to mass fluctuation and strain field fluctuation, respectively [50]. The calculation details are shown in the Supporting Information. For the D term, we estimated the value range of parameter E from reported materials in literatures. According to the calculation of F. Bridges et al. [49], the structural disorder scattering coefficient E for clathrates $\text{Eu}_8\text{Ga}_{16}\text{Ge}_{30}$ and $\text{Sr}_8\text{Ga}_{16}\text{Ge}_{30}$ are 9.52×10^{-16} s and 1.70×10^{-16} s, respectively. The degree of disorder for $\beta\text{-Ag}_9\text{FeS}_{4.5}\text{Te}_{1.5}$ is obviously higher than that of clathrates, whereas the degree of disorder for $\alpha\text{-Ag}_9\text{FeS}_4\text{Te}_2$ is very low. Therefore, the parameter E for $\beta\text{-Ag}_9\text{FeS}_{4.5}\text{Te}_{1.5}$ is set to be larger than 9.52×10^{-16} s, while the E for $\alpha\text{-Ag}_9\text{FeS}_4\text{Te}_2$ is set to be less than 1.70×10^{-16} s. For the RE term, we obtained the value of phonon resonance frequency ω_i through the formula $\hbar\omega_i = k_B \theta_{Ei}$ and then fixed it for the modelling of κ_L . Based on the above analysis, we fitted the low-temperature experimental κ_L of disordered $\text{Ag}_9\text{FeS}_{4.5}\text{Te}_{1.5}$ and ordered $\text{Ag}_9\text{FeS}_4\text{Te}_2$. The fitting results and contributions of different scattering mechanisms to the κ_L reduction are plotted in Fig. 5a and b. Fitting parameters are listed in Table S4. Obviously, the reduction of κ_L from grain boundary, point defect, and Umklapp process are very close in both compounds, whereas the main differences stem from the structural disorder

scattering and phonon resonant scattering.

As shown in Fig. 5, the reduction of κ_L attributed by structural disorder scattering (purple area) is much larger in disordered $\text{Ag}_9\text{FeS}_{4.5}\text{Te}_{1.5}$ than that in ordered $\text{Ag}_9\text{FeS}_4\text{Te}_2$. The highly structural disorder in $\text{Ag}_9\text{FeS}_{4.5}\text{Te}_{1.5}$ arises from a random occupation of the Ag sites, which breaks the lattice symmetry and periodicity and thus alters the phonon dispersion relations. Locally, such disorder not only substantially strengthens the phonon scattering but also changes the phonon group velocity as the phonon wave passes through the disordered atoms [49,51]. The disorder scattering term was introduced by Ziman [51] and subsequently applied to thermoelectrics by several groups [10,13,52,53].

The lowest resonant frequency of $\text{Ag}_9\text{FeS}_{4.5}\text{Te}_{1.5}$ is 2.5 THz, which is much lower than that (3.0 THz) of $\text{Ag}_9\text{FeS}_4\text{Te}_2$. The low-energy phonon resonant modes imply the presence of low-lying optical phonons, i.e., Einstein oscillators, which play a significant role in depressing the Debye frequency and suppressing κ_L . Meanwhile, the largest scattering coefficient C_i of $\text{Ag}_9\text{FeS}_{4.5}\text{Te}_{1.5}$ is $6.7 \times 10^{36} \text{ s}^{-3}$, which is dramatically higher than that ($1.1 \times 10^{36} \text{ s}^{-3}$) of $\text{Ag}_9\text{FeS}_4\text{Te}_2$. The larger scattering coefficient C_i indicates higher concentration of Einstein oscillators in $\text{Ag}_9\text{FeS}_{4.5}\text{Te}_{1.5}$. These two factors, i.e., low resonant frequency and high concentration of oscillators lead to the large reduction of κ_L (blue area in Fig. 5) in $\text{Ag}_9\text{FeS}_{4.5}\text{Te}_{1.5}$.

4. Conclusion

In summary, a series of $\text{Ag}_9\text{FeS}_{6-x}\text{Te}_x$ samples have been successfully synthesized and their phase compositions, crystal structures and especially thermal transport properties have been systematically investigated in this work. It is found that $\text{Ag}_9\text{FeS}_{6-x}\text{Te}_x$ has a wide chemical composition range with x from 0.5 to 2.0. The Ag^+ ions are weakly bonded to the surrounding S/Te anions in either ordered α -phase or disordered β -phase of $\text{Ag}_9\text{FeS}_{6-x}\text{Te}_x$. This consequently gives rise to the low energy multi-Einstein oscillators as corroborated by both experimental results and theoretical calculations. Compared to the ordered α -phase, the disordered β -phase possesses larger structural disorder, lower resonant frequency and higher concentration of oscillators, which contribute more to the reduction of κ_L . As a result, the κ_L of ordered α -phase exhibits a crystalline Umklapp peak at around 10 K, while the κ_L of disordered β -phase monotonously increases in the whole temperature range. This work attests to the significant role of structural disorder and weak chemical bonds in dominating ultralow κ_L of solid materials and provides guidelines for the design of high-performance thermoelectrics.

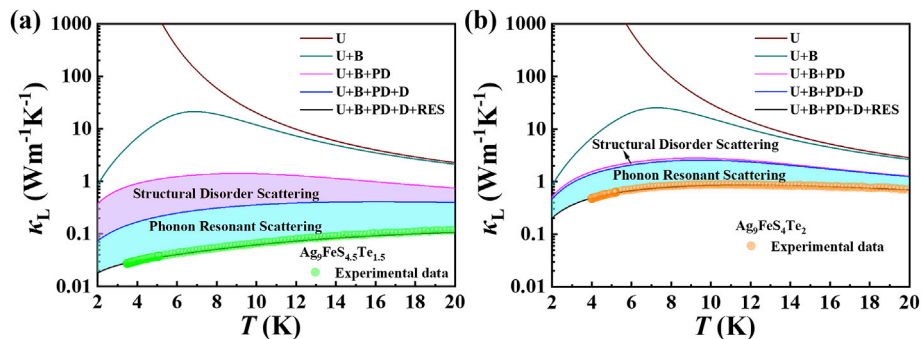


Fig. 5. Contributions of various phonon scattering mechanisms to the reduction of lattice thermal conductivity (κ_L) in (a) $\text{Ag}_9\text{FeS}_{4.5}\text{Te}_{1.5}$ and (b) $\text{Ag}_9\text{FeS}_4\text{Te}_2$. U, B, PD, D and RE denote the phonon–phonon Umklapp process, grain boundary scattering, point defect scattering, structural disorder scattering and phonon resonant scattering, respectively. The purple and blue areas highlight the contributions of structural disorder scattering and phonon resonant scattering to the reduction of κ_L , respectively.

Declaration of competing interest

The authors declare that they have no known competing financial interests or personal relationships that could have appeared to influence the work reported in this paper.

Acknowledgements

This work is supported by the National Key Research and Development Program of China (2018YFB0703600), the National Natural Science Foundation of China (51625205 and 51632010), and the Key Research Program of Chinese Academy of Sciences (KFZD-SW-421). K.Z. thanks for the support by the National Natural Science Foundation of China under Grant No. 51902199 and Shanghai Sailing Program (19YF1422800).

Appendix A. Supplementary data

Supplementary data to this article can be found online at <https://doi.org/10.1016/j.mtphys.2021.100410>.

Data availability

The raw/processed data required to reproduce these findings are available from the corresponding author on reasonable request.

Credit author statement

Zhicheng Jin: Methodology, Validation, Formal analysis, Investigation, Data curation, Writing – original draft, Visualization. Yifei Xiong: Software. Kungpeng Zhao: Conceptualization, Methodology, Writing – review & editing, Project administration, Funding acquisition. Hongliang Dong: Resources. Qingyong Ren: Resources. Hui Huang: Formal analysis. Xianxiu Qiu: Formal analysis. Jie Xiao: Resources. Pengfei Qiu: Conceptualization. Lidong Chen: Conceptualization, Funding acquisition. Xun Shi: Conceptualization, Writing – review & editing, Supervision, Funding acquisition.

References

- [1] G.J. Snyder, E.S. Toberer, *Nat. Mater.* 7 (2008) 105–114.
- [2] J. He, T.M. Tritt, *Science* 357 (2017): eaak9997.
- [3] X.-L. Shi, J. Zou, Z.-G. Chen, *Chem. Rev.* 120 (2020) 7399–7515.
- [4] F. Hu, S. Wu, Y. Sun, *Adv. Mater.* 31 (2018) 1801001.
- [5] N.P. Padture, *Science* 296 (2002) 280–284.
- [6] K. Biswas, J. He, I.D. Blum, C.-I. Wu, T.P. Hogan, D.N. Seidman, V.P. Dravid, M.G. Kanatzidis, *Nature* 489 (2012) 414–418.
- [7] L.D. Zhao, H.J. Wu, S.Q. Hao, C.I. Wu, X.Y. Zhou, K. Biswas, J.Q. He, T.P. Hogan, C. Uher, C. Wolverton, V.P. Dravid, M.G. Kanatzidis, *Energy Environ. Sci.* 6 (2013) 3346.
- [8] L. Hu, Y. Zhang, H. Wu, J. Li, Y. Li, M. McKenna, J. He, F. Liu, S.J. Pennycook, X. Zeng, *Adv. Energy Mater.* 8 (2018) 1802116.
- [9] P.C. Wei, C.N. Liao, H.J. Wu, D. Yang, J. He, G.V. Biesold-McGee, S. Liang, W.T. Yen, X. Tang, J.W. Yeh, Z. Lin, J.H. He, *Adv. Mater.* 32 (2020) 1906457.
- [10] K. Zhao, P. Qiu, Q. Song, A.B. Blichfeld, E. Eikeland, D. Ren, B. Ge, B.B. Iversen, X. Shi, L. Chen, *Mater. Today Phys.* 1 (2017) 14–23.
- [11] K. Zhao, P. Qiu, X. Shi, L. Chen, *Adv. Funct. Mater.* 30 (2019) 1903867.
- [12] Z. Zhang, K. Zhao, T.-R. Wei, P. Qiu, L. Chen, X. Shi, *Energy Environ. Sci.* 13 (2020) 3307–3329.
- [13] H. Liu, X. Shi, F. Xu, L. Zhang, W. Zhang, L. Chen, Q. Li, C. Uher, T. Day, G.J. Snyder, *Nat. Mater.* 11 (2012) 422–425.
- [14] Y. Wu, Z. Chen, P. Nan, F. Xiong, S. Lin, X. Zhang, Y. Chen, L. Chen, B. Ge, Y. Pei, *Joule* 3 (2019) 1276–1288.
- [15] R. Hanus, M.T. Agne, A.J.E. Rettie, Z. Chen, G. Tan, D.Y. Chung, M.G. Kanatzidis, Y. Pei, P.W. Voorhees, G.J. Snyder, *Adv. Mater.* 31 (2019) 1900108.
- [16] S. Lee, K. Esfarjani, T. Luo, J. Zhou, Z. Tian, G. Chen, *Nat. Commun.* 5 (2014) 3525.
- [17] L.-D. Zhao, S.-H. Lo, Y. Zhang, H. Sun, G. Tan, C. Uher, C. Wolverton, V.P. Dravid, M.G. Kanatzidis, *Nature* 508 (2014) 373–377.
- [18] S. Lin, W. Li, S. Li, X. Zhang, Z. Chen, Y. Xu, Y. Chen, Y. Pei, *Joule* 1 (2017) 816–830.
- [19] S.-H. Lo, J. He, K. Biswas, M.G. Kanatzidis, V.P. Dravid, *Adv. Funct. Mater.* 22 (2012) 5175–5184.
- [20] E.J. Skoug, D.T. Morelli, *Phys. Rev. Lett.* 107 (2011) 235901.
- [21] P. Ying, X. Li, Y. Wang, J. Yang, C. Fu, W. Zhang, X. Zhao, T. Zhu, *Adv. Funct. Mater.* 27 (2017) 1604145.
- [22] S. Wang, Y. Sun, J. Yang, B. Duan, L. Wu, W. Zhang, J. Yang, *Energy Environ. Sci.* 9 (2016) 3436–3447.
- [23] W. Li, S. Lin, M. Weiss, Z. Chen, J. Li, Y. Xu, W.G. Zeier, Y. Pei, *Adv. Energy Mater.* 8 (2018) 1800030.
- [24] X. Shen, Y. Xia, C.C. Yang, Z. Zhang, S. Li, Y.H. Tung, A. Benton, X. Zhang, X. Lu, G. Wang, J. He, X. Zhou, *Adv. Funct. Mater.* 30 (2020) 2000526.
- [25] W. Li, S. Lin, B. Ge, J. Yang, W. Zhang, Y. Pei, *Adv. Sci.* 3 (2016) 1600196.
- [26] X. Qi, J. Chen, K. Guo, S. He, J. Yang, Z. Li, J. Xing, J. Hu, H. Luo, W. Zhang, J. Luo, *Chem. Eng. J.* 374 (2019) 494–501.
- [27] D. Frank, B. Gerke, M. Eul, R. Pöttgen, A. Pfizner, *Chem. Mater.* 25 (2013) 2339–2345.
- [28] B. Jiang, P. Qiu, E. Eikeland, H. Chen, Q. Song, D. Ren, T. Zhang, J. Yang, B.B. Iversen, X. Shi, L. Chen, *J. Mater. Chem. C* 5 (2017) 943–952.
- [29] K.S. Weldert, W.G. Zeier, T.W. Day, M. Panthöfer, G.J. Snyder, W. Tremel, *J. Am. Chem. Soc.* 136 (2014) 12035–12040.
- [30] B. Jiang, P. Qiu, H. Chen, J. Huang, T. Mao, Y. Wang, Q. Song, D. Ren, X. Shi, L. Chen, *Mater. Today Phys.* 5 (2018) 20–28.
- [31] S. Lin, W. Li, Z. Bu, B. Gao, J. Li, Y. Pei, *Mater. Today Phys.* 6 (2018) 60–67.
- [32] J.P. Perdew, K. Burke, M. Ernzerhof, *Phys. Rev. Lett.* 77 (1996) 3865–3868.
- [33] A. Togo, I. Tanaka, *Scripta Mater.* 108 (2015) 1–5.
- [34] K. Zhao, E. Eikeland, D. He, W. Qiu, Z. Jin, Q. Song, T.R. Wei, P. Qiu, J. Liu, J. He, B.B. Iversen, J. He, L. Chen, X. Shi, *Joule* 5 (2021) 1–13.
- [35] S.I. Kim, K.H. Lee, H.A. Mun, H.S. Kim, S.W. Hwang, J.W. Roh, D.J. Yang, W.H. Shin, X.S. Li, Y.H. Lee, G.J. Snyder, S.W. Kim, *Science* 348 (2015) 109–114.
- [36] Y. Pei, X. Shi, A. LaLonde, H. Wang, L. Chen, G.J. Snyder, *Nature* 473 (2011) 66–69.
- [37] L. Song, J. Zhang, B.B. Iversen, *J. Mater. Chem.* 5 (2017) 4932–4939.
- [38] W.X. Zhou, Y. Cheng, K.Q. Chen, G. Xie, T. Wang, G. Zhang, *Adv. Funct. Mater.* 30 (2019) 1903829.
- [39] F.B. Lewis, N.H. Saunders, *J. Phys. C Solid State Phys.* 6 (1973) 2525–2532.
- [40] K. Zhao, C. Zhu, P. Qiu, A.B. Blichfeld, E. Eikeland, D. Ren, B.B. Iversen, F. Xu, X. Shi, L. Chen, *Nano Energy* 42 (2017) 43–50.
- [41] G.S. Nolas, G.A. Slack, D.T. Morelli, T.M. Tritt, A.C. Ehrlich, *J. Appl. Phys.* 79 (1996) 4002.
- [42] R.C. Zeller, R.O. Pohl, *Phys. Rev. B* 4 (1971) 2029–2041.
- [43] M. Jin, S.Q. Lin, W. Li, Z.W. Chen, R.B. Li, X.H. Wang, Y.X. Chen, Y.Z. Pei, *Chem. Mater.* 31 (2019) 2603–2610.
- [44] S.Q. Lin, W. Li, Z.L. Bu, B. Shan, Y.Z. Pei, *ACS Appl. Energy Mater.* 3 (2020) 1892–1898.
- [45] T. Takabatake, K. Suekuni, T. Nakayama, E. Kaneshita, *Rev. Mod. Phys.* 86 (2014) 669–716.
- [46] I.K. Dimitrov, M.E. Manley, S.M. Shapiro, J. Yang, W. Zhang, L.D. Chen, Q. Jie, G. Ehlers, A. Podlesnyak, J. Camacho, Q. Li, *Phys. Rev. B* 82 (2010) 174301.
- [47] J. Callaway, *Phys. Rev.* 113 (1959) 1046–1051.
- [48] J. Yang, D.T. Morelli, G.P. Meisner, W. Chen, J.S. Dyck, C. Uher, *Phys. Rev. B* 67 (2003) 165207.
- [49] F. Bridges, L. Downward, *Phys. Rev. B* 70 (2004) 140201.
- [50] K. Zhao, A.B. Blichfeld, H. Chen, Q. Song, T. Zhang, C. Zhu, D. Ren, R. Hanus, P. Qiu, B.B. Iversen, F. Xu, G.J. Snyder, X. Shi, L. Chen, *Chem. Mater.* 29 (2017) 6367–6377.
- [51] J. Ziman, D. Thouless, *Models of Disorder: the Theoretical Physics of Homogeneously Disordered Systems*, 1979.
- [52] H. Wang, A.D. LaLonde, Y. Pei, G.J. Snyder, *Adv. Funct. Mater.* 23 (2013) 1586–1596.
- [53] W.G. Zeier, Y. Pei, G. Pomrehn, T. Day, N. Heinz, C.P. Heinrich, G.J. Snyder, W. Tremel, *J. Am. Chem. Soc.* 135 (2013) 726–732.
- [54] D. Wu, L.-D. Zhao, S. Hao, Q. Jiang, F. Zheng, J.W. Doak, H. Wu, H. Chi, Y. Gelbstein, C. Uher, C. Wolverton, M. Kanatzidis, J. He, *J. Am. Chem. Soc.* 136 (2014) 11412–11419.
- [55] M. Beekman, D.G. Cahill, *Cryst. Res. Technol.* 52 (2017) 1700114.
- [56] H. Liu, J. Yang, X. Shi, S.A. Danilkin, D. Yu, C. Wang, W. Zhang, L. Chen, *J. Materiomics* 2 (2016) 187–195.
- [57] D.G. Cahill, S.K. Watson, R.O. Pohl, *Phys. Rev. B* 46 (1992) 6131–6140.